

A new low-mass eclipsing binary: NSVS 02502726[☆]

Ö. Çakırlı^{*,a}, C. İbanoğlu^a, C. Güngör^a

^aEge University, Science Faculty, Department of Astronomy and Space Sciences, 35100 Bornova, İzmir, Turkey

Abstract

We present optical spectroscopy and extensive *RI* differential photometry of the double-lined eclipsing binary NSVS 02502726 (2MASS J08441103+5423473). Simultaneous solution of two-band light curves and radial velocities permits determination of precise empirical masses and radii for both components of the system. The analysis indicates that the primary and secondary components of NSVS 02502726 are in a circular orbit with 0.56-day orbital period and have stellar masses of $M_1=0.714\pm0.019 M_\odot$, and $M_2=0.347\pm0.012 M_\odot$. Both of the components have large radii, being $R_1=0.645\pm0.006 R_\odot$, and $R_2=0.501\pm0.005 R_\odot$. The principal parameters of the mass and radius of the component stars are found with an accuracy of 3% and 1%, respectively. The secondary component's radius is significantly larger than model predictions for its mass, similar to what is seen in almost all of the other well-studied low-mass stars which belong to double-lined eclipsing binaries. Strong H_α emission cores and considerable distortion at out-of-eclipse light curve in both *R* and *I* bandpasses, presumably due to dark spots on both stars, have been taken as an evidence of strong stellar activity. The distance to system was calculated as 173 ± 8 pc from the *BVRIJHK* magnitudes. The absolute parameters of the components indicate that both components are close to the zero-age main-sequence. Comparison with current stellar evolution models gives an age of 126 ± 30 Myr, indicating the stars are in the final stages of pre-main-sequence contraction.

Key words: stars:activity-stars:fundamental parameters-stars:low mass-stars:binaries:eclipsing

1. Introduction

Most of the investigations made to determine the fundamental properties of low-mass stars using eclipsing binaries indicate a strong discrepancy between theory and observations. Radii measurements of the low-mass stars can be made from the eclipsing binaries plus interferometry of single stars. These measurements clearly indicate that the observed radii are generally larger than the predictions by the stellar models. On the other hand the observed temperatures are lower than those of predicted by the models. This discrepancy, the observed larger radii and lower temperatures, is generally explained by the high level of stellar activity.

Accurate parameters of low-mass stars are difficult to obtain, with the best source of precise data being double-lined eclipsing binaries, but those systems are not only scarce but also intrinsically faint. Therefore their detection is slightly difficult. As pointed out by Coughlin and Shaw

[☆]Based on photometric and spectroscopic observations collected at TÜBİTAK National Observatory (Turkey)

*Corresponding author

Email address: omur.cakirli@ege.edu.tr (Ö. Çakırlı)

12 (2007) only three low-mass double-lined eclipsing binary systems were known before 2003:
13 CM Dra (Lacy, 1977 and Metcalfe et al. 1996), YY Gem (Leung and Schneider 1978, Torres and
14 Ribas 2002) and CU Cnc (Delfosse et al. 1999, Ribas 2003). In the following five years the
15 number of low-mass systems has tripled by many variability surveys: BW5 V038 (Maceroni and
16 Montalbán 2004), TrES-Her 0-07621 (Creevey et al. 2005), GU Boo (Lopez-Morales and Ribas
17 2005), 2MASS J05162281+2607387 (Bayles and Orosz 2006), NSVS01031772 (Lopez-Morales
18 et al. 2006), UNSW-TR-2 A and B (Young et al. 2006), and 2MASS J04463285+1901432 A
19 and B in the open cluster NGC 1647 (Hebb et al. 2006). Thereafter, seven new low-mass eclipsing
20 binaries were discovered by Coughlin and Shaw (2007). Very recently Lopez-Morales et
21 al. (2006) discussed a plausible correlation between the magnetic activity levels, the metallicities
22 and the radii of low mass stars which depends on the precise radii measurements of 34 low
23 mass stars from the eclipsing binary systems. Ribas and colleagues (Ribas et al. 2003, Morales
24 et al. 2008) have revealed that the low-mass stars are systematically larger and cooler than the
25 predictions of theoretical calculations. However, there is no significant difference between the
26 observed and theoretical luminosities of the low-mass stars.

27 Clearly, the sample size of well-studied low-mass binaries needs to be increased. Since the
28 number of well-studied low-mass binaries is still relatively small, observations of additional low
29 mass binaries would be extremely useful. Light variability of the star known as NSVS 02502726
30 (hereafter NSVS 0250) was revealed by Wozniak et al. (2004) from the Northern Sky Variability
31 Survey. Later on it has been discovered to be an eclipsing binary by Coughlin & Shaw (2007).
32 Their preliminary study shows that NSVS 0250 consists of two dissimilar low-mass stars with
33 a joint apparent visual magnitude of $V_{rotse}=13.41$ and an orbital period of ~ 0.6 days. Since
34 spectroscopic observations are not available, they presented the photometric light curves and
35 preliminary models based only on the light curve analysis.

36 In this work we present follow-up photometric and spectroscopic observations of NSVS 0250
37 which confirm the low-mass nature of the component stars. We derive accurate fundamental
38 parameters for the component stars and compare our results with theoretical evolutionary models.

39 2. Observations and reductions

40 2.1. Differential photometry

41 We report here new photometry of NSVS 0250 in the Bessell R and I bands. Both the pho-
42 tometric accuracy (a few millimagnitudes) and the phase coverage (over 1000 observations)
43 are sufficient to guarantee a reliable determination of the light curve parameters. The obser-
44 vations were carried out with the 0.40 m telescope between January and February of 2008
45 at the TÜBİTAK National Observatory (TUG, located on Mt. Bakırlitepe, Antalya in south
46 of Turkey). The telescope is equipped with an Apogee 1k×1k CCD (binned 2×2) and standard
47 Bessell R and I filters.

48 The instrument with attached camera provides a field-of-view of $11'.3 \times 11'.3$. NSVS 0250
49 is a relatively faint target, with not many other objects of similar spectral type or brightness
50 nearby. By placing NSVS 0250 very close to center of the CCD to get the highest accuracy, we
51 managed to strategically locate the binary on the chip together with two other stars of similar
52 apparent magnitudes. We selected GSC 3798-1250 as a comparison star, located $1'.479$ away
53 from the target. The check star was GSC 3798-1234, at an angular distance of about $3'.047$ from
54 NSVS 0250, $2'.629$ from the comparison star. Both stars passed respective tests for intrinsic pho-
55 tometric variability and proved to be stable during time span of our observations. The variable,
56 comparison and check stars are shown in Figure 1.

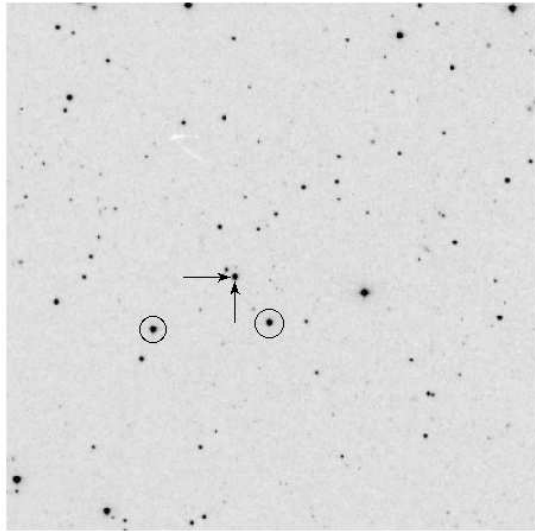


Figure 1: A $11'.3 \times 11'.3$ I band image of the field of NSVS 0250 showing the two comparison stars. The position of NSVS 0250 is indicated by vectors directed by east and north.

Table 1: Times of minima measured from the *BVRI*-band light curves. Caution: the first two columns should be shifted to the right.

| E | Type | HJD | O-C |
|------|------|------------|---------|
| 0.50 | II | 54497.2696 | -0.0007 |
| 1.00 | I | 54497.5502 | 0.0000 |
| 2.50 | II | 54498.3894 | -0.0005 |
| 3.00 | I | 54498.6701 | 0.0003 |
| 4.00 | I | 54499.2300 | 0.0004 |
| 4.50 | II | 54499.5085 | -0.0010 |
| 6.50 | II | 54500.6284 | -0.0007 |
| 8.00 | I | 54501.4690 | 0.0002 |

57 We collected a total of 1190 differential magnitudes in the *R*-band and 1235 in the *I*-band
58 with an exposure time of 10 seconds. The observations covered the entire orbit of the binary
59 in each filter. Machine-readable copies of the data are available in the electronic edition (see
60 supplementary material section of this article). Standard IRAF¹ tasks were used to remove the
61 electronic bias and to perform the flat-fielding corrections. The IRAF task *IMALIGN* was used
62 to remove the differences in the pixel locations of the stellar images and to place all the CCD
63 images on the same relative coordinate systems. The data were analyzed using another IRAF
64 task *PHOT* without taking into account differential extinction effects due to the relatively small
65 angular separation between the target, comparison and check stars on the sky.

66 2.1.1. Orbital period and ephemeris

Coughlin & Shaw (2007) observed seven low-mass detached systems, including NSV0250, with the Southeastern Association for Research in Astronomy (SARA) 0.9 m telescope in the Johnson *V*, *R* and *I* filters. The first orbital period and zero epoch for NSVS 0250 were determined from these observations. An orbital period of $P=0.559772\pm 0.000007$ days, and an initial epoch $T_0(\text{HJD})=2453692.0280\pm 0.0003$ for the mid-primary eclipse were calculated using a least square fit. To define the accurate period of NSVS 0250, We collected times of minima available from the literature and added 8 times of mid-eclipse obtained in this study, including 4 primary and 4 secondary. Accurate times for those mid-eclipses were computed by applying 6th order polynomial fits to the data during eclipses. The times of mid-eclipse obtained by us are listed in Table 1. A linear least squares fit to the obtained so far yields an orbital period of $P=0.559755\pm 0.000001$ days, which is 1.5 s shorter than that estimated by Coughlin & Shaw (2007). As the new reference epoch, we have adopted the first time of mid-primary eclipse that we observed, i.e. $T_0(\text{HJD})=2454497.5502\pm 0.0003$. The ephemeris of the system is now,

$$\text{Min } I(\text{HJD}) = 24\,54497.5502(3) + 0.559755(1) \times E. \quad (1)$$

67 Using these light elements we find an average phase difference between mid-primary and mid-
68 secondary eclipses $\Delta\phi=0.4992\pm 0.0008$, which is consistent with a circular orbit.

¹IRAF is distributed by the National Optical Observatory, which is operated by the Association of the Universities for Research in Astronomy, inc. (AURA) under cooperative agreement with the National Science Foundation

69 2.2. *Echelle spectroscopy*

70 Optical spectroscopic observations of NSVS 0250 (30 spectra) were obtained with the Turk-
71 ish Faint Object Spectrograph Camera (TFOSC) instrument attached to the 1.5 m telescope on
72 3 nights on 21, 22, 23 February 2008 under good seeing conditions. The TFOSC instrument
73 equipped with a 2048² pixel CCD was used. Further details on the telescope and the instru-
74 ment can be found at <http://www.tug.tubitak.gov.tr>. The wavelength coverage of each spectrum
75 is 4200-8700 Å in 11 orders, with a resolving power of $\lambda/\Delta\lambda$ 6000 at 6563 Å and an average
76 signal-to-noise ratio (S/N) of ~140. We also obtained a high S/N spectrum of the M dwarf GJ
77 410 (M0 V) and GJ 361 (M1.5 V) for use as a template in derivation of the radial velocities
78 (Nidever et al. 2002). By using a real star as template we avoid the problems that the low-mass
79 stellar atmosphere models have been reproducing some spectral features of the stars.

80 The electronic bias was removed from each image and we used the 'creject' option for
81 cosmic ray removal. This worked very well, and the resulting spectra were largely free from
82 cosmic rays. The echelle spectra were extracted and wavelength calibrated by using FeAr lamp
83 source with help of the IRAF ECHELLE package.

84 The stability of the instrument was checked by cross correlating the spectra of the standard
85 star against each other using the FXCOR task in IRAF. The standard deviation of the differences
86 between the velocities measured using fxcor and the velocities in Nidever et al. (2002) was about
87 1.1 km s⁻¹.

88 In the present work, the radial velocities of the components of NSVS 0250 were derived by
89 means of cross-correlation functions (CCFs) using the IRAF task fxcor (e.g. Tonry & Davis
90 1979). We used the spectra of the M dwarfs GJ 410 and GJ 361 as trial templates instead of the
91 synthetic spectra, the common procedure for massive stars. The reason behind this decision is
92 that the synthetic spectra computed using stellar atmosphere models reproduce well the spectral
93 features observed in real stars down to 0.60-0.65 M_{\odot} ($T_{eff} \leq 4000$ K), as is for example the case
94 of the H₂O molecule. To avoid the incompleteness of the models we used the spectra of real stars
95 with spectral type similar to the components of the binary.

96 Fig. 2 shows examples of CCFs at various orbital phases. The two peaks, non-blended, cor-
97 respond to each component of NSVS 0250. The stronger peaks in each CCF correspond to the
98 more luminous component that have a larger weight into the observed spectrum. We adopted a
99 two-Gaussian fit algorithm to resolve cross-correlation peaks near the first and second quadra-
100 tures when spectral lines are visible separately.

101 Near the quadrature phases, absorption lines of the primary and secondary components of
102 the system can be easily recognized in the range between 4200-6800 Å. We limited our analysis
103 to the echelle orders in the spectral domains 4200-6800 Å, which include several photospheric
104 absorption lines. We have disregarded very broad lines like H α , H β and H γ because their broad
105 wings affect the CCF and lead to large errors. A double-lined Gaussian fit was used to disentangle
106 the CCF peaks and determine the RVs of each component. Following the method proposed
107 by Penny et al. (2001) we first made two-Gaussian fits of the well separated CCFs using the
108 deblending procedure in the IRAF routine SPLOT. The average fitted FWHM is 200±12, and
109 190±10 km s⁻¹ for the primary and secondary components, respectively. In Fig. 3 we show a
110 sample of double-Gaussian fit. Indeed, the shapes and velocities corresponding to the peaks of
111 the CCFs are slightly changed. By measuring the areas enclosed by the Lorentian profiles of the
112 spectral lines belonging to the primary (A_1) and secondary (A_2) we estimate the light ratio of the
113 primary star to the secondary as 1.613. Using this light ratio we find $\frac{L_1}{(L_1+L_2)}=0.617$.

114 The heliocentric RVs for the primary (V_p) and the secondary (V_s) components are listed
115 in Table 2, along with the dates of observation and the corresponding orbital phases computed

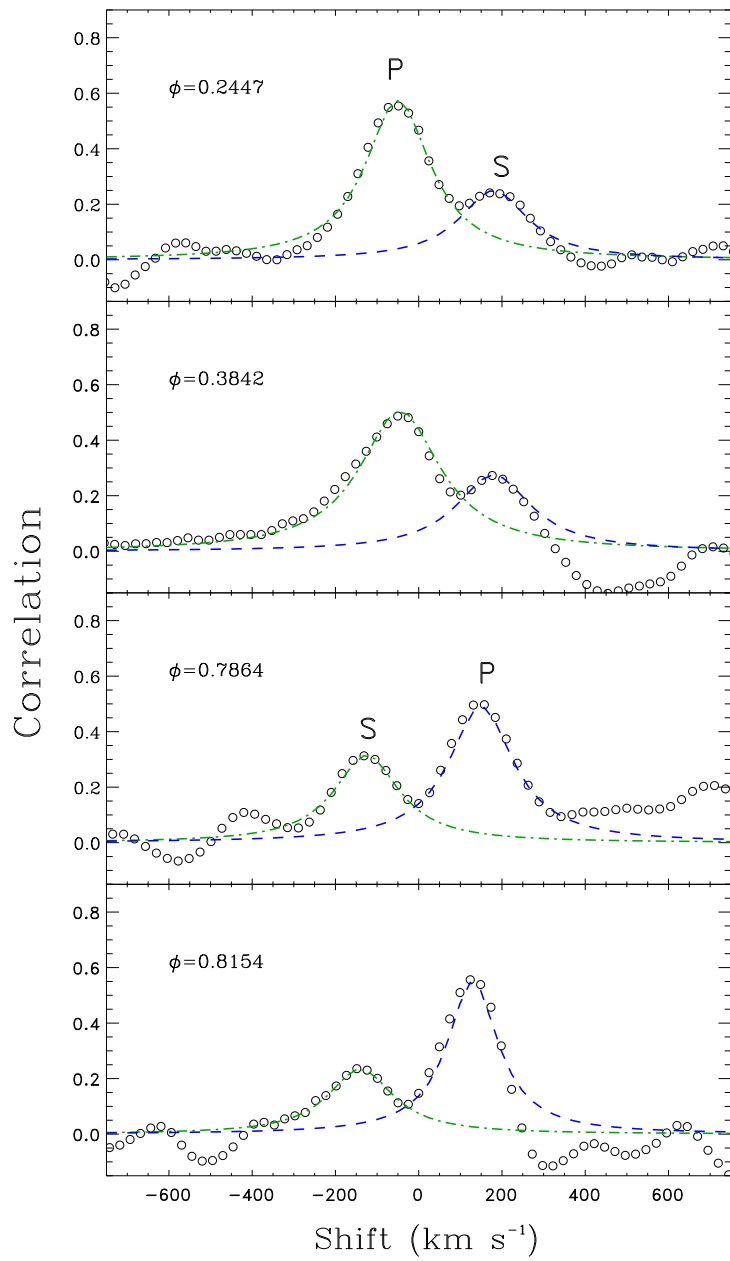


Figure 2: Sample of Cross Correlation Functions (CCFs) between NSVS 0250 and the radial velocity template spectrum around the first and second quadrature.

Table 2: Heliocentric radial velocities of NSVS 0250. The columns give the heliocentric Julian date, the orbital phase (according to the ephemeris in Eq. 1), the radial velocities of the two components with the corresponding standard deviations.

| HJD 2400000+ | Phase | Star 1 | | Star 2 | |
|--------------|--------|--------|----------|--------|----------|
| | | V_p | σ | V_s | σ |
| 54518.3468 | 0.1530 | -67.7 | 6.3 | 132.5 | 11.8 |
| 54518.3805 | 0.2132 | -78.7 | 4.6 | 178.1 | 8.8 |
| 54518.4122 | 0.2699 | -61.3 | 8.8 | 177.8 | 9.1 |
| 54518.4525 | 0.3419 | -67.7 | 9.7 | 170.5 | 7.0 |
| 54518.4980 | 0.4232 | -30.9 | 15.7 | 99.5 | 14.7 |
| 54518.5804 | 0.5704 | 31.9 | 18.9 | -67.0 | 10.9 |
| 54518.6232 | 0.6468 | 78.5 | 11.1 | -125.7 | 6.6 |
| 54519.2611 | 0.7864 | 91.6 | 4.6 | -163.2 | 4.3 |
| 54519.2684 | 0.7995 | 92.4 | 8.9 | -154.7 | 6.7 |
| 54519.2975 | 0.8515 | 86.0 | 7.1 | -136.7 | 7.7 |
| 54519.3416 | 0.9302 | 55.2 | 15.7 | -78.4 | 12.4 |
| 54519.4336 | 0.0946 | -29.5 | 19.9 | 114.1 | 18.4 |
| 54519.4797 | 0.1770 | -71.1 | 3.5 | 161.8 | 6.7 |
| 54519.5191 | 0.2473 | -70.7 | 5.5 | 189.7 | 8.9 |
| 54519.5476 | 0.2983 | -73.0 | 7.8 | 179.5 | 11.9 |
| 54519.5957 | 0.3842 | -45.4 | 5.8 | 129.4 | 8.8 |
| 54519.6400 | 0.4633 | -15.3 | 14.6 | 62.0 | 17.6 |
| 54520.3968 | 0.8154 | 88.6 | 6.6 | -146.3 | 7.6 |
| 54520.4551 | 0.9195 | 55.7 | 11.2 | -84.8 | 11.5 |
| 54520.5454 | 0.0808 | -27.2 | 19.7 | 91.0 | 12.3 |
| 54520.5694 | 0.1237 | -54.4 | 14.4 | 114.1 | 9.8 |
| 54520.6371 | 0.2447 | -77.7 | 6.6 | 185.1 | 10.8 |

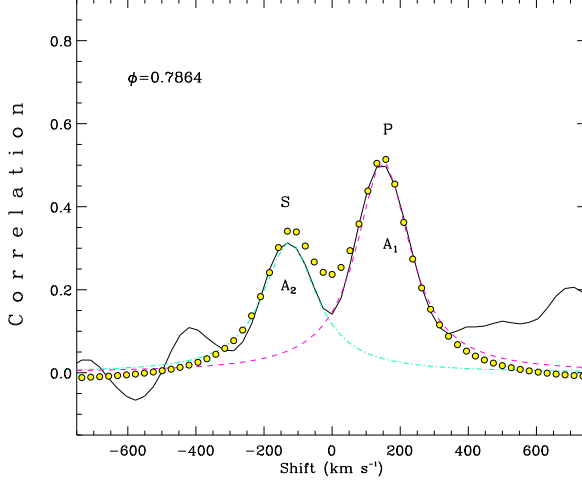


Figure 3: Sample of “deblending” a triple-peaked cross-correlation function (CCF) between NSVS0250 and template spectrum GJ410 at $\phi=0.7833$ (showing clear double-lined profile in figure). P, and S refer to primary, secondary components, respectively. The fit to the observed spectrum for the P and S made up by two Lorentian function is shown by dots. All radial velocities of the primary and secondary have been measured by excluded of the deblending effect using this way. The deconvolved two gaussian profiles of the primary and secondary component are displayed by dashed and dot-dashed line in the figure.

116 with the new ephemeris given in §2.1.1 The velocities in that table have been corrected to the
 117 heliocentric reference system by adopting a radial velocity of -13.9 km s^{-1} for the template star
 118 GJ 410 (Giese 1991). The RVs listed in Table 2 are the weighted averages of the values obtained
 119 from the cross-correlation of orders #4, #5, #6 and #7 of the target spectra with the corresponding
 120 order of the standard star spectrum. The weight $W_i = 1/\sigma_i^2$ has been given to each measurement.
 121 The standard errors of the weighted means have been calculated on the basis of the errors (σ_i)
 122 in the RV values for each order according to the usual formula (e.g. Topping 1972). The σ_i
 123 values are computed by `FXCOR` according to the fitted peak height, as described by Tonry & Davis
 124 (1979). The observational points and their error bars are displayed in Fig. 4 as a function of the
 125 orbital phase. We measure the semi-major axis $a=2.939\pm0.027 R_\odot$ and semi-amplitudes of the
 126 RVs of more massive primary and the less massive secondary components to be $K_1 = 86 \pm 3 \text{ km}$
 127 s^{-1} and $K_2 = 177 \pm 4 \text{ km s}^{-1}$, respectively.

128 3. Analysis

129 3.1. System variability

130 The light curves obtained by us in the *I* and *R* badpasses are distinctly different from the light
 131 curves obtained by Coughlin & Shaw (2007) in the same badpasses . Their *VRI* light curves were
 132 shown in Figure 2 (hereafter Fig. 2X) in that paper. The light curves are nearly symmetric in
 133 shape, showing the system slightly brighter at second quarter than at the first quarter. The asym-
 134 metry is better distinguished at the shorter wavelengths. The primary and secondary eclipses are
 135 deeper in the *I*-band, being 0.88 and 0.41 mag, respectively. The *R* and *I*-band light curves of the

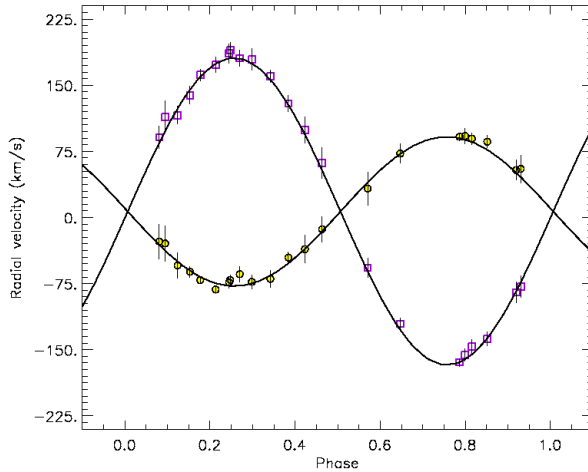


Figure 4: Radial velocity curve folded on a period of 0.5598 days, where phase zero is defined to be at primary mid-eclipse. Symbols with error bars (error bars are masked by the symbol size in some cases) show the RV measurements for two components of the system (primary: open circles, secondary: open squares).

136 system obtained by us show considerable out-of-eclipse variability with an amplitude of about
 137 0.07 mag, presumably due to cool spots on one or both stars. Asymmetries in the light curves are
 138 known as common feature of low-mass eclipsing binaries (e.g. the GU Boo light curves shown
 139 by Lopez-Morales & Ribas 2005). However, the activity level in NSVS0250 seems to be the
 140 same compared to other well-studied low mass binaries (see §4.2). If the light variations at out-
 141 of-eclipses are due to spots, substantial portion of the surface of one or both components would
 142 have been covered with dark spots.

143 3.2. Light curve modeling

144 We modeled the light curves and radial velocities using the Wilson-Devinney (WD) code
 145 implemented into the PHOEBE package by Prsa & Zwitter (2005). The modified version of this
 146 program allows one to calculate radial velocities and multiple light curves of stars simultane-
 147 ously, either for a circular or an eccentric orbit, in a graphical environment. In this model the
 148 code was set in Mode-2 for detached binaries with no constraints on their surface potentials. The
 149 simplest assumptions were used for modeling the stellar parameters: the stars were considered
 150 to be black bodies and the approximate reflection model (MREF=1) was adopted. The gravity
 151 darkening exponents were set 0.32 according to the mean stellar temperatures given by Claret
 152 (2000). The bolometric albedos of 0.5 for each star were taken, which correspond to stars with
 153 convective envelopes. We assume a circular orbit with synchronous rotation for both stars.

154 Since the light curve is asymmetric in shape we attributed it to spots (either bright and dark)
 155 on one or both components. The spots in the PHOEBE are parameterized in the same way as in
 156 the Wilson-Devinney (1971) code. They are circular regions specified by four parameters: the
 157 "temperature factor" T_f , the "latitude" of the spot center, the "longitude" of the spot center, and
 158 the angular radius of the spot. Bright spots have $T_f > 1$ and dark spots have $T_f < 1$.

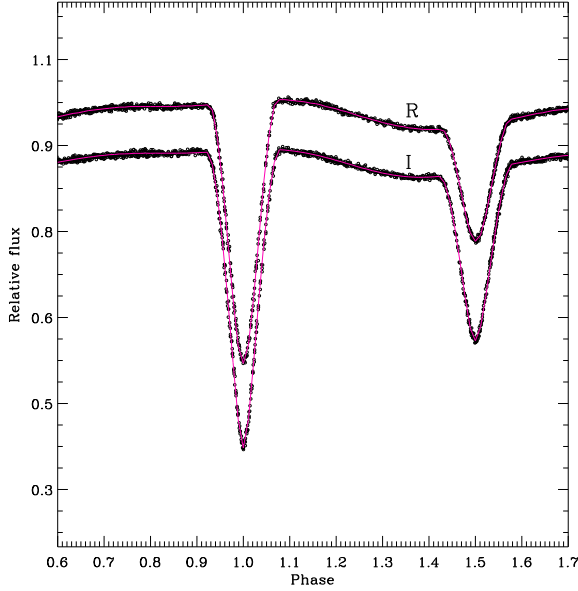


Figure 5: The light curve model (solid lines) composed with our I and R-band photometry.

159 The effective temperature of the primary component of the eclipsing pair was derived from
 160 the calibrations of Drilling & Landolt (2000) using preliminary estimate of its mass. The primary
 161 component of the eclipsing pair seems to have a mass of $0.71 M_{\odot}$ which corresponds to a spectral
 162 type of about K3 with an effective temperature of 4650 K. On the other hand, the infrared colours
 163 of NSVS 0250 given in the 2MASS catalogue (Skrutskie 1999) as $H - K = 0.154$ and $J - H = 0.584$
 164 mag which correspond to an effective temperature of 4300 K in the infrared colors-effective
 165 temperature relations given by Tokunaga (2000). Therefore we started light curve analysis with
 166 an effective temperature of the hotter component of 4300 K.

167 We followed two steps to determine the binary parameters. First, the inclination, the effective
 168 temperature of the secondary star (T_2), and potentials (stellar radii) were iteratively adjusted
 169 within PHOEBE until both the depths and duration of the eclipses are matched with the observed
 170 *R* and *I* light curves. The iteration was carried out automatically until convergence is obtained, i.e.
 171 as the set of parameters for which the differential corrections were smaller than the probable
 172 errors.

173 Since the light curve of the system has a wave-like distortion we tried to represent it by
 174 cool spots on the components. The shape of the distortion curve depends on the number of spots,
 175 locations and sizes on the stars' surface. Hundreds of trials indicated that one spot on the primary
 176 and two spots on the secondary component could reproduce the distortion on the light curve. The
 177 temperature of the secondary component, $T_2 = 3620 \pm 205$, has been derived from the temperature
 178 ratio provided by the analysis of the light curve. The effective temperature of 3620 K for the less
 179 massive component corresponds to an M2 star.

180 We fit our photometric data with model light curves using the spot parameters given in Table

181 3. No satisfactory fit was possible without starspots, moderate cool spots were added one at a
 182 time, with typical temperature factors, $T_f = \frac{T_{spot}}{T_{photophere}}$, of about 0.85, 0.78 and 0.94. In Fig. 5, the
 183 computed light curves with one spot on the primary and two spots on the secondary star, given
 184 in Table 3, are compared with observed R - and I -band light curves.

185 4. Summary and conclusion

186 4.1. Absolute parameters of the components

187 Combining the parameters of the photometric and spectroscopic orbital solutions we derived
 188 absolute parameters of the stars. The standard deviations of the parameters have been determined
 189 by JKABSDIM² code, which calculates distance and other physical parameters using several
 190 different sources of bolometric corrections (Soutworth et al. 2005a). The best fitting parameters
 191 are listed in Table 3 together with their standard deviations.

192 The ratio of the temperatures of the stars is consistent with their mass and radius ratios. How-
 193 ever, a more accurate determination of the mean absolute temperature of NSVS 0250's secondary
 194 is still necessary. Note that the potentially large uncertainty in the adopted effective temperature
 195 of the primary and calculated for the secondary has no impact on the accuracy of the determined
 196 absolute dimensions. For example, the radii of the stars, which are obtained from the light curve
 197 modelling, suffer in appreciable changes when T_{eff} values moderate uncertainty about the mean
 198 one adopted.

199 The luminosity and absolute bolometric magnitudes M_{bol} of the stars in Table 4 were com-
 200 puted from their effective temperatures and their radii. Since low-mass stars radiates more energy
 201 at the longer wavelengths we used $RJJK$ magnitudes given by Coughlin & Shaw (2007). Ap-
 202 plying $UBVRIJKL$ brightness- T_{eff} relations given by Kervella et al. (2004) we calculated the
 203 distance to NSVS 0250 as $d = 173 \pm 8$ pc.

204 The mean light contribution of the primary star $\frac{L_1}{(L_1+L_2)} = 0.62$ obtained from the R -band light
 205 curve analysis is in agreement with that estimated from the FWHM as 0.62. On the other hand we
 206 find a light contribution of the primary component as 0.61 using the absolute parameters given
 207 in Table 4. This indicates that light contributions of the spotted primary component, computed
 208 by three different ways, are very close to each other.

209 4.2. H_α emission profiles

210 The H_α line is an important indicator of photospheric and chromospheric activity in the low-
 211 mass stars. Very active binaries show H_α emission above the continuum (e.g. SDSS-MEB-
 212 1, Blake et al. 2007); in less active stars a filled-in absorption line is observed. For some
 213 objects the H_α line goes from filled-in absorption to emission during flare events as shown in YY
 214 Gem (Young et al. 1989). In the spectra of NSVS 0250 collected by us clearly indicated strong
 215 emission in H_α for both components above the continuum in some orbital phases. However, in
 216 some orbital phases the H_α lines appear to be very shallow absorption, i.e. filled-in absorption
 217 line, below the continuum. In Fig. 6 we show H_α emission features in some orbital phases
 218 together with their equivalent width variation (bottom panel) as a function orbital phase. We find
 219 a clear evidence of the H_α -line equivalent width (EW) variation with the orbital phase, indicating
 220 direct emission with larger EW when the spotted areas are visible. Such correlation between the

²This can be obtained from <http://http://www.astro.keele.ac.uk/~jkt/codes.html>

Table 3: Properties of the NSVS 0250 components.

| # | Parameters | Value |
|------------|--------------------------------|---------------|
| | P^a (days) | 0.559755 |
| | T_0^a (HJD) (Min I) | 24 54497.5502 |
| | γ (km s ⁻¹) | 3.15±0.44 |
| | $q = \frac{m_2}{m_1}$ | 0.486±0.010 |
| | i° | 87±1 |
| | a (R _⊙) | 2.914±0.026 |
| | K_1 (km s ⁻¹) | 86±3 |
| | K_2 (km s ⁻¹) | 177±4 |
| | $L_1/(L_1 + L_2)_R$ | 0.6200±0.0010 |
| | $L_1/(L_1 + L_2)_I$ | 0.3800±0.0009 |
| | Ω_1 | 4.8037±0.0021 |
| | Ω_2 | 3.8624±0.0034 |
| | r_1 | 0.2312±0.0005 |
| | r_2 | 0.2619±0.0008 |
| | T_{eff_1} (K) | 4 300[Fix] |
| | T_{eff_2} (K) | 3 620±205 |
| | rms | 0.044 |
| Spot1 | <i>Star location</i> | Primary |
| parameters | Latitude (deg) | 37 |
| | Longitude (deg) | 254 |
| | Angular radius (deg) | 38 |
| | $T_{spot}/T_{photosphere}$ | 0.85 |
| Spot2 | <i>Star location</i> | Secondary |
| parameters | Latitude (deg) | 39 |
| | Longitude (deg) | 261 |
| | Angular radius (deg) | 54 |
| | $T_{spot}/T_{photosphere}$ | 0.78 |
| Spot3 | <i>Star location</i> | Secondary |
| parameters | Latitude (deg) | 22 |
| | Longitude (deg) | 141 |
| | Angular radius (deg) | 57 |
| | $T_{spot}/T_{photosphere}$ | 0.94 |

^a See §2.1.1

Table 4: The absolute parameters of the components of NSVS0250.

| Parameter | Primary | Secondary |
|----------------------------|-------------------|-------------------|
| Mass (M_{\odot}) | 0.714 ± 0.019 | 0.347 ± 0.012 |
| Radius (R_{\odot}) | 0.674 ± 0.006 | 0.763 ± 0.007 |
| Temperature (K) | $4\,300 \pm 200$ | $3\,620 \pm 205$ |
| Luminosity (L_{\odot}) | 0.139 ± 0.014 | 0.090 ± 0.010 |
| $\log g$ (cgs) | 4.635 ± 0.004 | 4.213 ± 0.008 |
| M_{bol} (mag.) | 6.88 ± 0.14 | 7.35 ± 0.12 |
| M_V (mag.) | 7.73 ± 0.13 | 9.11 ± 0.14 |
| Distance (pc) | 173 ± 8 | |

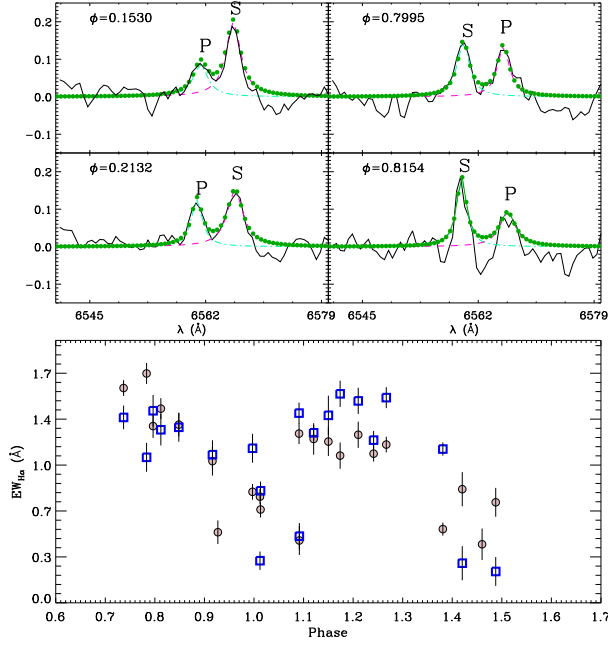


Figure 6: Sample deblending of the double-peaked H_{α} emission spectra of NSVS 0250 (top panels). The fit to the observed spectrum (continuous line) made up by two Lorentian function is shown by dots. The deconvolved emission profiles of the primary and secondary component are displayed by dashed and dot-dashed line, respectively. In the bottom panel we show equivalent variation of the H_{α} -line versus the orbital phase. The symbols square and circle denote the EWs of the secondary and primary component, respectively.

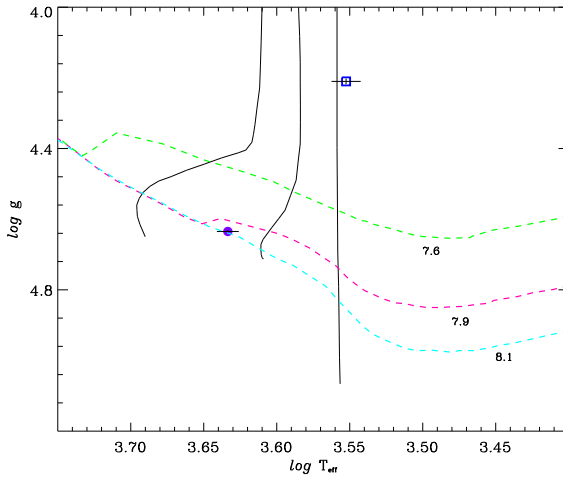


Figure 7: Location of the primary (filled circle) and secondary (open square) stars in the theoretical H-R diagram. The components of NSVS 0250 compared to mass-tracks and isochrones from Palla and Stahler (1999) models. The solid lines are mass-tracks of masses 0.4, 0.6, 0.8 M_{\odot} . The dashed lines are $[M/H]=0$ isochrones of ages $\log t=7.6$, 7.9, and 8.1 years.

221 EWs of H_{α} -line and orbital phase is known for chromospherically active RS CVn-type stars for
 222 a long time.

223 Our observations of NSVS 0250 are well distributed in orbital phase and were obtained at
 224 a spectral resolution 0.9 \AA . Both components display H_{α} emission cores and the more massive
 225 component usually shows weaker emission. Four spectra of NSVS 0250 in the deblending of
 226 a double-peaked H_{α} region show emission core from both stars in any case for the comparable
 227 intensities of the components. The radial velocities of the components could be measured from
 228 the deblending H_{α} emission lines, near the orbital phases of 0.25 and 0.75. These RVs are very
 229 close to those obtained from the absorption lines, indicating that the H_{α} emission lines are formed
 230 in a region close to the stars' surface.

231 The relevant result of the simultaneous photometric and H_{α} monitoring is that the less mas-
 232 sive and cooler star appears also as the more active at a chromospheric level, since it has a larger
 233 H_{α} -line's EWs at this epoch. Therefore, one can conclude that the secondary component should
 234 be more heavily spotted, which is confirmed by the light curve analysis.

235 4.3. HR diagram

236 We can now compare the fundamental stellar parameters derived from the orbital solution
 237 (Table 4) inferred currently available theoretical evolutionary models. This comparison may
 238 easily be done by comparing location of a star in the $\log T_{eff}$ vs. $\log g$ or mass-radius diagrams
 239 formed by theoretical predictions. As an example, Fig. 7 shows the locations of the primary
 240 and secondary stars on the theoretical HR diagram, i.e. $\log T_{eff}$ vs. $\log g$. The evolutionary
 241 tracks for the pre-main sequence stars with masses of 0.8, 0.6 and $0.4 M_{\odot}$ taken from Palla and
 242 Stahler (1999) are also plotted for comparison. The location of the primary component in the \log
 243 T_{eff} vs. $\log g$ diagram is in agreement with theoretical prediction of a $0.7 M_{\odot}$. Using the solar

244 metallicity models, we find a best-fit age for the primary star of $\sim 126 \pm 30$ Myr. The uncertainty
 245 of the age has been estimated from the errors in the effective temperature and surface gravity of
 246 the primary star. On contrary the secondary component seems to have an age of about 10 Myr,
 247 indicating too young with respect to the primary star. This contradiction may be arisen from
 248 the very large radius, therefore smaller surface gravity, of the secondary component. On the
 249 other hand, when compared the locations of the components in the $\log T_{eff}$ vs. $\log L$ diagram,
 250 while the primary component appears to be on the evolutionary track of a $0.7 M_{\odot}$ the secondary
 251 star is seen to be having higher luminosity, therefore younger. Such tests of low-mass stellar
 252 models have been carried out by a number of authors in the past. Torres & Ribas (2002) and
 253 Ribas (2003) have systematically pointed out a discrepancy between the stellar radii predicted
 254 by theory and the observations. Model calculations appear to underestimate stellar radii by \sim
 255 10 %, which is a highly significant difference given the observational uncertainties. Recently,
 256 Ribas et al. (2003) and Morales et al. (2008) made a comparison between the mass-radius
 257 and mass- T_{eff} relations predicted by models and the observational data for stars below $1 M_{\odot}$
 258 from detached eclipsing binaries. They conclude that current stellar models predict radii for
 259 low-mass stars 10% smaller than measured. Furthermore the computed effective temperatures
 260 are 5% larger, while the luminosities are in agreement. While the radius of the more massive
 261 component is in agreement with the stars with same masses, the secondary component seems to
 262 have 1.5 times larger with respect to its mass than predicted by the stellar theory for an age of the
 263 primary star (see Morales 2007, Figure 1). This is the reason why the location of the secondary
 264 component does deviate from the predicted in the $\log T_{eff}$ vs. $\log g$ diagram. Morales et al.
 265 (2008) indicate that chromospherically active stars are cooler and larger than the inactive stars of
 266 similar luminosity. Even if the use of $\log T_{eff}$ vs. $\log L$ diagram, the cooler temperatures will of
 267 course lead to infer younger ages even the $\log T_{eff}$ vs. $\log L$ diagram is used.

268 The heliocentric space velocity components of NSVS0250 were computed from its position,
 269 radial velocity (γ), distance (d), and proper motion. The latter were retrieved from the *2MAS*
 270 catalogue ($\mu_{\alpha}, \mu_{\delta}$). The resulting space velocity components are (U,V,W)³; U= -1.7 ± 0.2 km s⁻¹,
 271 V= 1.6 ± 0.3 km s⁻¹, W= 2.6 ± 0.1 km s⁻¹, which correspond to a total space velocity of S= 4.1 ± 0.9
 272 km s⁻¹. We can infer from those space velocities that NSVS 0250 should not be an older star.
 273 Therefore, we conclude that the system seems to have an age of about 126 Myr. Both components
 274 are in the final stages of the pre-main-sequence contraction.

275 5. Acknowledgements

276 The authors acknowledge generous allotments of observing time at TUBITAK National Ob-
 277 servatory of Turkey. We also wish to thank the Turkish Scientific and Technical Research Coun-
 278 cil for supporting this work through grant Nr. 108T210 and EBİLTEM Ege University Sci-
 279 ence Foundation Project No:08/BİL/0.27. This research has been made use of the ADS-CDS
 280 databases, operated at the CDS, Strasbourg, France.

281 References

282 [] Bayless A. J. and Orosz J. A., 2006, ApJ, 651, 1155

³According to our convention, positive values of U, V, and W indicate velocities towards the galactic center, galactic rotation and north galactic pole, respectively.

283 [] Blake C. H., Torres G., Bloom J. S., and Gaudi B. S., 2007, arXiv0707.3604v1
284 [] Claret A., 2000, A&A, 359, 289
285 [] Coughlin J. L., and Shaw J. S., 2007, JSARA, 1, 7C
286 [] Creevey O. L. et al., 2005, ApJL, 625, 127
287 [] Delfosse X., Forveille T., Mayor M., Burnet M., and Perier C., 1999, A&A, 341, L63
288 [] Drilling J. S., Landolt A.U., 2000, Allen's Astrophysical Quantities, Fouth Edition, ed. A.N.Cox (Springer), p.388
289 [] Girardi L., Bressan A., Bertelli G., and Chiosi C., 2002, A&AS, 141, 371
290 [] Hebb L., Wyse R. F. G., Gilmore G. and Holtzman J., 2006, AJ, 131, 555
291 [] Kervella P., Segransan D., Coude du Foresto V., 2004, A&A, 425, 116
292 [] Lacy C. H., 1977, ApJ, 218, 444
293 [] Leung K. C. and Schneider D. P., 1978, AJ, 83, 618
294 [] Lopez-Morales M. et al., 2006, ApJ, submitted, [arXiv:astro-ph/0610225]
295 [] Lopez-Morales M. and Ribas I., 2005, ApJ, 631, 1120
296 [] Maceroni C. and Montalban J., 2004, A&A, 426, 577
297 [] Metcalfe T., S., Mathieu R. D., Latham D. W., and Torres G., 1996, ApJ, 456, 356
298 [] Morales J. C., Ribas I., and Jordi C., 2008, A&A, 478, 507
299 [] Nidever D. L., Marcy G. W., Butler R. P., Fischer D. A., and Vogt S. S., 2002, ApJS, 141, 503
300 [] Penny R. L. et al., 2001, ApJ, 548, 889
301 [] Palla F., and Stahler S. W., 1999, ApJ, 525, 772
302 [] Prsa A. and Zwitter T., 2005, ApJ 628, 426
303 [] Ribas I., 2003, A&A, 398, 239
304 [] Southworth J., Clausen J. V., 2005, A&A, 461, 1077
305 [] Skrutskie M. F. et al., 1999, AJ, 131, 1163
306 [] Torres G. and Ribas I., 2002, ApJ, 567, 1140
307 [] Tonry J. and Davis M., 1979, AJ 84, 1511
308 [] Topping J., 1972, "Errors of Observation and Their Treatment", (Chapman and Hall Ltd.), p.89
309 [] Tokunaga A. T., 2000, "Allen's astrophysical quantities", Fouth Edition, ed. A.N.Cox (Springer), p.143
310 [] Wozniak P. R. et al., 2004, AJ, 127, 2436
311 [] Wilson R.E. and Devinney E.J., 1971, ApJ, 166, 605
312 [] Young T. B., Hidas M. G., Webb J. K., Ashley M. C. B., Christiansen J. L., Derekas A. and Nutto C., 2006,
313 MNRAS, 370, 1529
314 [] Young A., Skumanich A., Stauffer J. R., Harlan E., Bopp B. W., 1989, ApJ, 344, 427